Journal of Materials Chemistry A

A Rechargeable Liquid Metal-CO_2 Battery for Energy Storage and CO^2 Reduction to Carbon

Journal:	*Journal of Materials Chemistry A*
Manuscript ID	TA-COM-01-2024-000254
Article Type:	Communication
Date Submitted by the Author:	12-Jan-2024
Complete List of Authors:	Gabski, Jan; University of Cincinnati, Department of Chemical and Environmental Engineering Sun, Xinhui; University of Cincinnati, Chemical and Environmental Engineering Iskhakova, Landysh; University of Cincinnati, Chemical and Environmental Engineering Dong, Junhang; University of Cincinnati, Chemical Engineering/SEEBME

COMMUNICATION

A Rechargeable Liquid Metal-CO_2 Battery for Energy Storage and CO_2 Reduction to Carbon

Received 00th January 20xx,
Accepted 00th January 20xx

DOI: 10.1039/x0xx00000x

Jan Gabski, Xinhui Sun, Landysh Iskhakova, Junhang Dong *

A new type of high-temperature liquid gallium-CO_2 battery (LGaCB) is demonstrated to overcome the major limitations of slow reaction kinetics and inactive solid blockage of electrodes associated with the current solid metal-CO_2 batteries (MCBs). The LGaCB has exhibited power densities that are over an order of magnitude higher than the best of existing MCBs. The LGaCB operates by unique mechanisms enabled by CO_3^{2-} conduction through molten carbon electrolyte and Ga self-catalyzed CO_2 reduction, which discharge Ga_2O_3 nanoparticles (dia. ~ 20 nm) and large chunks of carbon (>50μm) in the liquid Ga (LGa). In the charging process, the Ga_2O_3 nanoparticles dispersed in the LGa is reduced without significant reverse oxidation of carbon that leads to an overall carbon-negative effect.

1 Introduction

Electric energy storage (EES) and catalytic CO_2 reduction (CO_2R) technologies can play enabling roles in achieving energy and environmental sustainability through the utilization of renewable energy. In the past decade, various metal–CO_2 batteries (MCBs) have shown great potential for EES with simultaneous CO_2R capability. [1] To date, several metal anolytes have been demonstrated for MCBs, including the alkali metals (Li, Na, and K), Mg, Zn, and Al, etc. The MCBs of highly reactive alkali metals typically employed nonaqueous electrolytes and produced carbon and metal carbonates by cathodic CO_2R while those of less reactive Mg, Zn and Al allowed operation with aqueous electrolytes to generate a variety of carbonaceous pieces from the cathodic CO_2R. [2-5] However, the cathodic CO_2R involves multiple electron transfer steps with high activation energy barriers, which impose severe kinetic limitations at low temperatures. [6,7] Moreover, the existing MCBs discharge resistive solids such as carbonates, oxides, and carbon at the gas(CO_2)/electrolyte/electrode triple-phase boundaries (TPBs) to hinder the mass and electric charge transfer in charging and discharging processes. [8,9]

Thus, discovering innovative heterogeneous electrochemical catalysts and catalyst architectures for enhancing the cathodic CO_2R reaction kinetics and transport efficiency has been the primary focus of MCB research. Various catalysts made of Pt-group metals (PGMs) and Au, functionalized composite nanomaterials, and nanostructured transition metals/alloys have been reported to reduce the reaction overpotentials. [2,4,10,11] In the past, the LiCBs were the most extensively studied type for their high energy density and cell potential. More recently, the ZnCBs were attracting growing interest for the possibility of better operability, lower costs, and flexible CO_2R product options but the discharge current density (i_{dch}), voltage (V_{dch}), and power density ($P_e = i_{dch} \cdot V_{dch}$) remained impractically low. [2,10,12] In summary, despite a decade of extensive research with many innovations in metal anolyte, gas electrode, and electrolyte, the inherent limitations of slow reaction and transport rates remain as major hurdles to achieving practically meaningful MCB performances.

Herein, we demonstrate a new kind of rechargeable high-temperature liquid gallium (LGa)-CO_2 battery (LGaCB), which uses CO_2/air mixture feeds to overcome the reaction kinetic limitations without using precious metals and circumvent the destructive solid deposition at the gas electrode surface. The LGaCB comprises a LGa anode (LGaA), which is also the liquid metal anolyte, a supported molten carbonate electrolyte (MCE) membrane, and a surface-oxidized nickel (NiO/Ni) gas(CO_2) electrode (NiGE). It is hypothesized that, when operating above the melting point (T_m) of the carbonate electrolyte (e.g.,

Department of Chemical and Environmental Engineering, University of Cincinnati, Cincinnati, OH 45221, USA. Email: dongj@ucmmail.uc.edu; Phone: +1 (513) 556-3992

* Corresponding author.

† Electronic Supplementary Information (ESI) available: SEM/EDS characterizations of the alumina supported MCE; SEM/EDS and XRD examinations of the NiGE; EIS measurements of the cell ASR as a time during LGaCB preparation; SEM/EDS, Raman, and XPS analyses of the solid products in LGa after MR operation under open-circuit; SEM and EDS results of Ga reaction in the air and CO_2 atmospheres; and OCV, polarization curve, and discharge characteristics of the LGaCB without supercharging cleaning after cell assembly. See DOI: 10.1039/x0xx00000x

>500°C), the cathodic reduction of O_2/CO_2 to CO_3^{2-} (1) at the Gas/MCE/NiGE TPBs, the CO_3^{2-} transfer through the MCE, and the anodic oxidation of Ga by CO_3^{2-} (2) at the LGaA/MCE interface can be thermally activated to overcome the kinetic resistances. The overall cell reaction (3), i.e., the Ga oxidation, has a standard potential of $E^o_{r,298K}$ = 1.72 V based on the Gibbs free energy of Ga_2O_3 formation, i.e., $\Delta G^o_{f,298K}$= – 998.3 kJ/mol. [13]

$$CO_2 + \frac{1}{2}O_2 + 2e^- \xrightarrow{NiO/Ni} CO_3^{2-} \quad (1)$$

$$2Ga + 3CO_3^{2-} \rightarrow Ga_2O_3 + 3CO_2 + 6e^- \quad (2)$$

$$2Ga + \frac{3}{2}O_2 \rightarrow Ga_2O_3 \quad (3)$$

The thermally activated reaction (1) on the NiGE and the CO_3^{2-} transfer through the MCE are similar to those occurring in the molten carbonate fuel cells (MCFCs). The LGa is chosen as the anolyte/anode because of its low T_m (~ 29.8°C), high boiling point (T_b ~ 2400°C), chemical stability and safety in ambient environments, and more importantly, its proven catalytic activity for CO_2R to carbon (CO_2RC) from room temperature to over 500°C. [14-16] Therefore, it is further hypothesized that the CO_2 molecules discharged by reaction (2) are individually in direct contact with the LGa for efficient Ga-catalyzed CO_2R to C and O_2 with the latter subsequently oxidizes Ga to give an overall reaction (4). [14,16]

$$2Ga + 3CO_2 \leftrightarrow Ga_2O_3 + 3C \quad (4)$$

Thus, unlike the conventional MCBs in which solids form at the gas electrode surfaces, the LGaCB generates solid carbon and Ga_2O_3 at the LGaA/MCE (liquid/liquid) interface that can be dispersed by the LGa to avoid blockage of electrode surfaces.

2 Experimental

The membrane-electrode assembly (MEA) of the LGaCB is schematically shown in Fig. 1a with the battery testing system and photos of the actual ceramic cell hosting the MEA are provided in Fig 1b. The MCE used was a eutectic mixture of Li_2CO_3 and K_2CO_3 with a Li/K atomic ratio of 0.62/0.38, i.e., $Li_{0.62}K_{0.38}CO_3$ overall, which has a T_m of ~ 498°C. [17] These NiGE and MCE are established electrode and electrolyte for MCFCs, which operate above the T_m of MCE (i.e.,>500°C) to achieve thermally activated cathodic reduction of O_2/CO_2 via the peroxide (O_2^{2-}) or superoxide (O_2^-) path and ion conduction by O_2^{2-} or O_2^- ion/CO_2 mixed diffusion, respectively. [18,19]

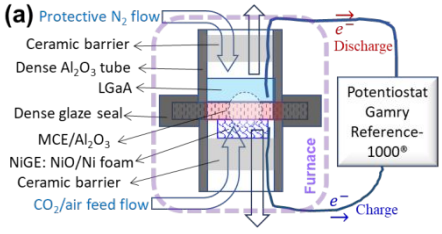

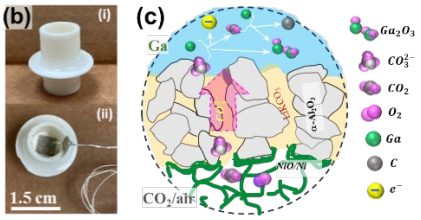

Fig. 1 (a) Schematic showing the LGaCB cell structure and the testing system, (b) photos of the actual cell showing (i) cathode and anode chambers of dense alumina tubes glazed to the MCE-loaded alumina disc and (ii) installation of the NiGE), and (c) an enlarged view showing the possible reaction and mass transport activities across the MEA.

A 0.6-mm-thick, porous a α-Al_2O_3 disc (porosity ε ~ 50%, pore dia. ~6 μm; Soilmoisture Equip. Corp, USA) was used to host the MCE. A piece of dense alumina tube (O.D. ~ 12 mm and I.D. ~ 1.0 mm) was mounted to each side of the alumina disc by ceramic glaze to serve as an electrode chamber (Fig. 1b). The NiGE was a 0.6cm×0.6cm sheet of 0.5-mm-thick Ni foam (99.7 % purity, Guangjiayuan New Material Inc., China), which was attached to the alumina disc by silver glue at its corners and connected to the potentiostat by a ϕ0.5-mm Ni wire (Fig. 1b). The active NiGE area was thus around 0.36 cm^2 and weighed ~3.2 mg in fresh state. The MCE loading was done by spreading a calculated amount of Li_2CO_3-K_2CO_3 mixture (Li:K = 0.62:0.38) over the disc and then heating up to 508°C and dwelling for 3 h when the molten carbonate infiltrated under capillary action to fully fill the pores in the alumina disc (Fig. S1). The MCE-loaded cell (Fig. 1b) was then cooled down to load the LGa (99.99% purity, Sigma-Aldrich, USA) on the disc surface that was opposite to the NiGE side. The LGa loads were 1097 mg(LGa)/cm^2 and 275 mg(LGa)/cm^2, which fully covered the disc with a thickness of 5 mm and 1.2 mm, respectively. These LGa amounts were estimated to ensure effective dispersion of the solid products and a secured contact between the electronically conducting LGa phase and the tip of a ϕ0.5mm Ni wire connected to the external circuit. A 1-cm long end segment of the Ni wire was gold-coated for mitigating the Ni surface oxidation or alloying and dissolving by the LGa. The tip of the Ni wire was fixed in the LGa layer at a position that was about 0.5 mm away from the MCE surface. The entire LGaCB cell was made of carbon-free materials except the MCE that ensured reliable analysis of the solid products in LGa.

The complete LGaCB assembly was reheated to 508°C with a 20 cm^3 (STP)/min N_2 flow purging the LGaA side to prevent air diffusion to the LGa and a feed containing 30v.% CO_2 and 70v.% air flowing through the NiGE side at a rate of 20 cm^3 (STP)/min under atmospheric pressure. This mixture composition was determined to obtain a O_2/CO_2 molar ratio of about 1:2, which is consistent with the stoichiometric ratio for reaction (1). The originally mounted fresh Ni foam was oxidized in-situ in the CO_2/air flow during the battery preparation and stabilization processes at 508°C to form a NiO surface layer, i.e., in a NiO/Ni structure (Fig. S2).

All LGaCB operations and tests were conducted at 508±3°C, which was slightly above T_m (498°C [17]) of the MCE under atmospheric pressure. The area specific resistance (ASR) of the MCE-loaded alumina disc was ~ 0.97 $\Omega \cdot cm^2$ under these conditions prior to LGa loading (Fig. S3a). The cell ASR increased

to ~2.6 Ω·cm² after loading the LGa and thermally stabilizing at 508°C (Fig. S3b). This significant increase of cell ASR could be attributed to the Ga_2O_3 formation at the MCE/NiGE interface. The LGaCB operated in membrane reactor (MR) mode under open circuit when the LGa could catalyze CO_2RC [16] for the CO_2 transported through the MCE. Under open circuit, the O_2 reduction (5) is at equilibrium state at the gas(CO_2/air)/MCE/NiGE TPB. [20] However, the CO_2 transport through MCE could be facilitated by the O_2^- or O_2^{2-} ion/CO_2 mixed diffusion when CO_2 was continually consumed by the overall reaction (4), which may include the LGa self-catalyzed endothermic CO_2RC (6a) and subsequent exothermic Ga oxidation by O_2 (6b). The reaction rate under the MR mode was expected to be limited by the back diffusion rate of O_2^- (or O_2^{2-}) due to the MCE's lack of electronic conductivity.

$$CO_3^{2-} + \frac{3}{2}O_2 \overset{NiO/Ni}{\longleftrightarrow} 2O_2^- + CO_2 \quad (5)$$

$$CO_2 \overset{Ga}{\rightarrow} C + O_2 \quad (6a)$$

$$2Ga + \frac{3}{2}O_2 \rightarrow Ga_2O_3 \quad (6b)$$

The LGa surface samples were taken after running the LGaCB in MR mode for 5 h. The SEM-EDS examinations (Fig. S4a) and Raman tests (Fig. S4b) of the samples confirmed that graphitic carbon and Ga_2O_3 particles formed in the LGa. The Ga 2p XPS spectra of the samples (Fig. S4c) also confirmed the oxidation of Ga to Ga^{3+} in open-circuit condition. Apparently, the Ga_2O_3 crystallized into nanosized needles and spheres in the LGa which were buoyed to the LGa surface. It could be inferred by the absence of carbonate peak in the C 1s spectrum at binding energy ~ 290 eV [21] (Fig. S4d) that $Ga_2(CO_3)_3$ was not a major product because the direct formation reaction $2Ga + 3CO_3^{2-} \rightarrow Ga_2(CO_3)_3 + 6e^-$ could not be sustained under open circuit due to the lack of e^- conductivity in the MCE.

The results of material analysis suggest mechanisms of reaction (5) at TPB and O_2^- or O_2^{2-} ion/CO_2 mixed diffusion through the MCE. [20] Thus, CO_2RC in MR mode could be accomplished either by the simple replacement reaction (4) or via the Ga-catalyzed CO_2 decomposition ($CO_2 \overset{Ga}{\rightarrow} C + O_2$) while the produced O_2 subsequently oxidized the Ga. The exact reaction routes are yet to be investigated because rapid Ga oxidation could be achieved at 508°C in both air and CO_2/N_2 (30v:70v) flows. The LGa oxidation in both atmospheres produced large agglomerates of Ga_2O_3 nanoparticles with primary grain diameters of ~50 nm in the former (Fig. S5a) and ~ 30 nm in the latter (Fig. S5b). However, the shapes of Ga_2O_3 particles from rapidly oxidizing directly in air and CO_2 atmospheres were very different from the nanoparticles obtained from LGaCB operation in MR mode, where Ga_2O_3 nucleation and crystal growth occurred in the LGa.

3 Results and discussion

The tests of the LGaCB conducted immediately after the 4-h heating-up and stabilization period only showed an open circuit voltage (OCV) of 0.6±0.15 V (Fig. S6a), a maximum power density ($P_e = V_{dch} \cdot i_{dch}$) of 3.75 mW/cm² as determined from the polarization curve (Fig. S6b), and a continued discharge P_e of 2 mW/cm² at i_{dch} ~ 9 mA/cm² (Fig. S6c). This performance was on par with the state-of-the-art MCBs in open reports. However, the OCV and P_e of the LGaCB were unexpectedly low that was likely caused by oxides and contaminations at the LGaA/MCE interface and connections to the MEA. The LGaCB could be effectively cleaned and activated by 8 min of supercharging at a high i_{ch} = 120 – 135 mA/cm² when the V_{ch} increased from 2.60 to 3.06 V (Fig. 2a). The thus activated LGaCB subsequently performed 4 cycles of discharge and charge at i_{dch} and i_{ch} of 10 mA/cm² (Fig. 2a) with an average V_{dch} of ~ 1.3 V (Fig. 2b) to provide a P_e of 13 mW/cm², which was much higher than the best of existing MCBs in the literature.

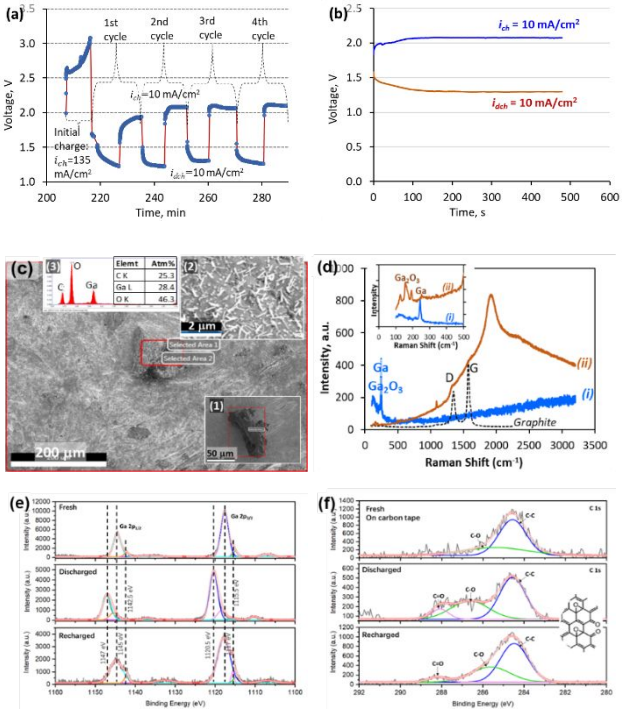

Fig. 2 Results of LGaCB operation: (a) four cycles of charge-discharge after an initial step of high-current charging (LGa load: 1097mg/cm²), (b) a representative charge and discharge cycle, (c) the SEM image of the discharged products (insert 1: a large carbon particle isolated from the products; insert 2: Ga_2O_3 nanoparticles; and insert 3: EDS element survey over the product sample), (d) Raman spectra of discharged sample indicating β-Ga_2O_3 [22] and graphite in the products: (i) spectrum of sample area free of carbon particles and (ii) spectrum of sample area with carbon particles, and (e) Ga 2p XPS spectra of fresh, discharged, and recharged LGa samples, and (f) C 1s spectra of the LGa samples on carbon tape for C-C peak reference.

The SEM image of the discharged LGa sample (Fig. 2c) showed large carbon particles (> 50 μm; insert 1) and nanosized Ga oxide needles and spheres with dia. <20 nm (insert 2). The EDS elemental survey over the area around large particles showed significant amounts of carbon and oxygen from the Ga oxides (Fig. 2c, insert 3). The Raman shift spectra for the samples from areas with and without features of very large carbon particles (Fig. 2d) revealed that the carbon and Ga oxides were mainly graphite and β-Ga_2O_3 [22], respectively. Furthermore, accumulation of carbon particles with the charge-discharge cycles was visually evident. This indicated that reactions in charging process were not the exact reverse of discharging

reactions and carbon products could be removed without disabling the LGaCB rechargeability.

The Ga 2p XPS spectra (Fig. 2e) of fresh, discharged, and recharged LGa samples showed significant shifts of binding energy from 1115.5 and 1145 eV towards 1120.5 and 1147 eV, respectively, after discharging, and reverse shifts to lower energy levels after recharging. The electrochemical reduction of Ga oxides formed by reaction with CO_2 at high temperature was also reported in the literature. [15] These confirmed that the redox cycle of $Ga \rightleftharpoons Ga^{3+}$ [23,24] enabled the discharge and charge processes. The C 1s XPS spectrum of the discharged sample (Fig. 2f) exhibited binding energy peaks for C-C, C-O, and carbonyl C=O, which are common in oxidized graphite surfaces. The characteristic peak of carbonate (i.e., O-C=O binding energy of ~289.5 eV [21]) was not appreciable in all samples. However, the involvement of $Ga_2(CO_3)_3$ as an intermediate product of discharge could not be ruled out because decomposition of $Ga_2(CO_3)_3$ could approach completion when the produced CO_2 molecules were instantaneously reduced by the surrounding Ga at high temperature. The timely consumption of CO_2 could also avoid the formation of CO, which was reported to occur via the reverse Boudouard reaction ($2CO \leftrightarrow CO_2 + C$) during Ga-catalyzed CO_2RC in CO_2-rich environments at ~ 500°C. [16]

Because Ga_2O_3 and carbon were generated at the LGaA/MCE interface, the cell ASR thus inevitably varied during the LGaCB operation. An identically made LGaCB was used to investigate charge-discharge behaviors at varied i_{dch} and i_{ch}, the temporal evolution of polarization curve, and changes of cell resistance through the continued operation (Fig. 3a). The cell was kept at 508°C under open-circuit MR mode until the resistance stabilized, after which an 8-min activating supercharge was performed at i_{ch} = 122 mA/cm² when V_{ch} increased from 2.4 to 3.0 V. A discharge-charge cycle was then performed at i_{dch} and i_{ch} of 10 mA/cm² (Fig. 3a insert), which exhibited a P_e of 12.8 mW/cm², a voltage gap ΔV_{gap} ~ 0.45 V. The LGaCB exhibited a round-trip voltage efficiency ($\eta_{d/ch} = V_{dch}/V_{ch}$) of about 74% that compared favorably with the existing MCBs (Fig. S7) considering that this was achieved at such high current and power densities. On the basis of cathode catalyst (fresh Ni) mass, the LGaCB achieved this good efficiency at i_{dch} (=i_{ch}) of 1124 mA/g(Ni) and P_e=1417 mW/g(Ni). In comparison, the highest MCB efficiency of 87.7% was reportedly achieved by an AlCB using a Pd-coated nanoporous gold (NPG@Pd) cathode only at i_{dch} (=i_{ch}) of 333 mA/g(NPG@Pd) and P_e=223 mW/g(NPG@Pd), which were much lower than those of the LGaCB.

Three polarization curves were measured after charging at 10 mA/cm and 122 mA/cm², respectively (Fig. 3b). Improvements in the maximum P_e (Fig. 3b) and reduction of cell ASR (Fig. 3c) were discernible after performing multiple discharging and charging processes at varied current densities. The progressively decreasing polarization along the operation steps (Fig. 3b) suggested continued improvements in dispersion and migration of the solid products away from the LGaA/MCE (liquid/liquid) interface to the LGa surface. The linear segments of the polarization curves showed cell ASR decreasing from ~48.2 at the beginning to ~15.5 $\Omega \cdot cm^2$ at the end of this multistep discharge/charge operation (Fig. 3c). The in-situ EIS measurements also indicated the same trend of ASR decrease from ~18.2 to ~7.5 $\Omega \cdot cm^2$ over the operation period. However, the ASR estimated from the polarization curves were much larger than the values measured by EIS because the former included significant contributions from mass transfer resistance and perhaps insufficient NiGE surface as well, which would not affect the EIS measurement of ohmic resistance under static condition. Thus, based on the effective cell ASR from the polarization curve, the reaction activation overpotential ($\Delta V_a = E_r - V_{dch} - i_{dch} \cdot ASR$) was estimated to be rather minor, which was only 0.008 V at a i_{dch} of 10 mA/cm² (detailed calculation given in SI). This minimal ΔV_a indicated that the reaction kinetic limitations were effectively overcome by thermal activation in the LGaCB, which is a common advantage of high-temperature fuel cells such as solid oxide fuel cells and MCFCs.

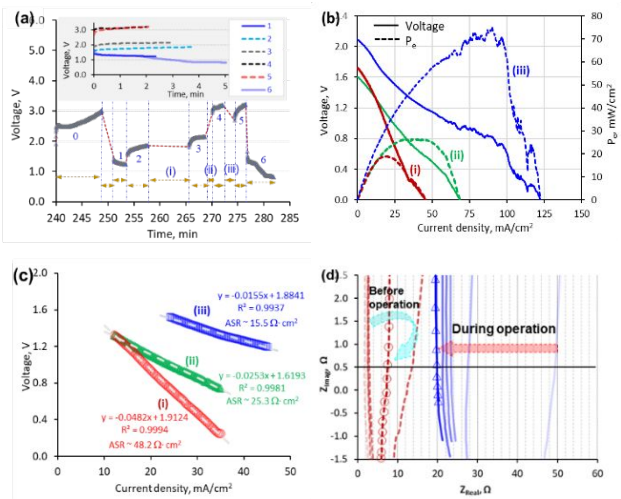

Fig. 3 LGaCB performance variation with charge-discharge operations: (a) continued cell tests including an initial supercharging activation at i_{ch} = 122 mA/cm² after the 4-h heating-up and cell stabilization period (LGa load: 275 mg/cm²) (1 – discharging at 10 mA/cm², 2 – charging at 10 mA/cm², (i) polarization curve, 3 – charging at 10 mA/cm², (ii) polarization curve, 4 – charging at 122 mA/cm², (iii) polarization curve, 5 – charging at 122 mA/cm², and 6 – discharging at 30 mA/cm²), (b) polarization curves and P_e dependency on i_{dch}, (c) cell resistance estimated from the linear segments of polarization curves, and (d) in-situ EIS measurements of the cell resistance before and during the charge/discharge operations.

Despite the large cell ASR, this LGaCB achieved a maximum P_e of ~75 mW/cm² that was more than 10 times the best of existing MCBs and demonstrated discharge at 30 mA/cm² with a P_e of 32.4 mW/cm², which were 6 times that of the best ZnCB in recent reports (Fig. 4).

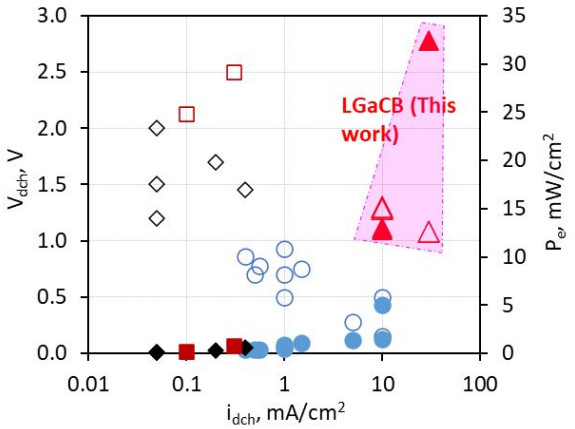

Fig. 4 Comparisons of the i_{dch}-dependent V_{dch} and P_e between the LGaCB and existing MCBs (open symbols represent V_{dch} and closed symbols represent P_e: ◊♦ LiCB [25]; □■ NaCB [14,26]; ○● ZnCB [11,12,27]; △▲ LGaCB of this work).

4 Conclusions

A rechargeable LGaCB was demonstrated at 508°C to overcome or circumvent the major limitations of slow reaction kinetics and solid blockage of gas electrode, which have hindered the development of existing low temperature MCBs. During the LGaCB discharge, CO_3^{2-} ions were generated from the CO_2/air feed by a simple NiGE and conducted through the MCE most likely via the O_2^- (or O_2^{2-}) and CO_2 mixed diffusion; the LGa was then oxidized by CO_3^{2-} at the LGaA/MCE interface to complete the cell operation. Ga_2O_3 nanoparticles (dia. ~ 20 nm) and very large graphite particles (>50μm) were discharged at the LGaA/MCE (liquid/liquid) interface and buoyed to the LGa surface presumably after certain accumulation that avoided physical blockage of the NiGE. In the charging process, Ga_2O_3 (Ga^{3+}) is reduced to Ga and oxygen ions (e.g., O_2^- or O_2^{2-}) apparently without total oxidation of carbon that led to realization of carbon-negative effect. The preliminary LGaCB achieved a maximum P_e of ~75 mW/cm^2, which was nearly 15 times the best of existing MCBs, and discharge at 30 mA/cm^2 with a P_e of 32.4 mW/cm^2, which were 6 times those of the best ZnCB in the latest reports. The findings of this work could open up opportunities for developing a new type of liquid metal MCBs to achieve practically relevant performance for simultaneous EES and CO_2RC with carbon-negative effects. The liquid metal anolyte may also permit flow battery operation mode to decouple the power and storage capacity while allowing external removal of the very large graphite particles but keeping the Ga_2O_3 nanoparticles circulated for Ga^{3+}/Ga redox cyclic operation. It is also worth noting that for developments practical devices, the current collector could use graphite plates for better stability, availability, and lower costs. The high temperature liquid metal-CO_2 batteries may find important applications in EES for combustion-based power plants and renewable energy systems with permanent carbon fixation via simultaneous CO_2RC.

Author Contributions

J.G.: investigation, validation, formal analysis, and data curation – battery fabrication and performance tests, material and chemical analyses, and data collection and processing. X.S.: investigation and formal analysis – material characterization, validation experiments, and data process. L.I.: investigation – instrumentation for battery tests and chemical analysis. J.D.: conceptualization, methodology, formal analysis, supervision, funding acquisition, and writing.

Conflicts of interest

There are no conflicts to declare.

Acknowledgements

This work is financially supported by the George Rieveschl Jr. Endowment Fund and the U.S. Department of Energy (DE-FE0031765).

Notes and references

1 C. Xu, Y. Dong, H. Zhao, Y. Lei, *Adv. Funct. Mater.,* 2023, 2300926.
2 J. Xie, X. Wang, J. Lv, Y. Huang, M. Wu, Y. Wang, J. Yao, *Angew. Chem. Int. Ed.,* 2018, **57**, 16996 –17001.
3 P. Ding, J. Zhang, N. Han, Y. Zhou, L. Jia, Y. Li, *J. Mater. Chem. A*, 2020, **8**, 12385.
4 C. Zhang, A. Wang, L. Guo, J. Yi, J. Luo, *Angew. Chem. Int. Ed*., 2022, **61**, e202200181.
5 M.K. Aslam, H. Wang, S. Chen, Q. Li, J. Duan, *Mater. Today Energy,* 2023, **31**, 101196.
6 Feng, N.; He, P.; Zhou, H. *Adv. Energy Mater.,* 2016, **6**(9), 1502303.
7 J. Wang, B. Marchetti, X. Zhou, S. Wei, *ACS Energy Lett.,* 2023, 8, 1818−1838.
8 J. Lin, W. Song, C. Xiao, J. Ding, Z. Huang, C. Zhong, J. Ding, W. Hu, *Carbon Energy,* 2023, **5**, e313.
9 X. Chen, J. Chen, Y. Liu, Y. Liu, Y. Gao, S. Fan, X. He, X. Liu, C. Chao, Y. Jiang, L. Li, Y. Qiao, S. Chou, *ACS Appl. Mater. Interfaces,* 2023, **15**, 28106−28115.
10 R. Yang, J. Xie, Q. Liu, Y. Huang, J. Lv, M.A. Ghausi, X. Wang, Z. Peng, M. Wu,Y. Wang, *J. Mater. Chem. A,* 2019, **7**, 2575–2580.
11 X. Wang, J. Xie, M.A. Ghausi, J. Lv, Y. Huang, M. Wu, Y. Wang, J. Yao, *Adv. Mater.,* 2019, **31**, 1807807; W. Ma, X. Liu, C. Li, H. Yin, W. Xi, R. Liu, G. He, X. Zhao, J. Luo, Y. Ding, Adv. Mater., 2018, **30**, 1801152; X. Hu, Z. Li, Y. Zhao, J. Sun, Q. Zhao, J. Wang, Z. Tao, J. Chen, *Sci. Adv.,* 2017, **3**, e1602396; S. Yang, Y. Qiao, P. He, Y. Liu, Z. Cheng, J. Zhu, H. Zhou, *Energy Environ. Sci.,* 2017, **10**, 972 – 978; F. Wang, Y. Li, X. Xia, W. Cai, Q. Chen, M. Chen, *Adv. Energy Mater.,* 2021, **11**, 2100667; W. Liu, X. Sui, C. Cai, H. Huang, R. Xu, D. Geng, M. Chen, J. Lu, *Adv. Energy Mater.,* 2022, **12**, 2201675; X. Li, G. Qi, J. Zhang, J. Cheng, B. Wang, *Adv. Funct. Mater.,* 2022, **32**, 2105029; B. Chen, X. Zhong, G. Zhou, N. Zhao, H.M. Cheng, *Adv. Mater.,* 2022, **34**, 2105812.
12 K. Wang, Y. Wu, X. Cao, L. Gu, J. Hu, *Adv. Funct. Mater.,* 2020, **30**, 1908965; S. Gao, Y. Liu, Z. Xie, Y. Qiu, L. Zhuo, Y. Qin, J. Ren, S. Zhang, G. Hu, J. Luo, X. Liu, *Small Methods,* 2021, **5**(4), e2001039; Y. Wang, L. Xu, L. Zhan, P. Yang, S.

Tang, M. Liu, X. Zhao, Y. Xiong, Z. Chen, Y. Lei, *Nano Energy,* 2022, **92**, 106780; H. Xie, H. Liao, S. Zhai, T. Liu, Y. Wu, F. Wang, J. Li, Y. Zhang, B. Chen, *Energy*, 2023, 263, 125688.
13 W.M. Haynes, ed. *CRC Handbook of Chemistry and Physics* (92nd ed.). Boca Raton, FL, CRC Press. 2011, pp 5-12.
14 H. Xie, H. Liao, S. Zhai, et. al, *Adv. Mater.,* 2022, **34**, 2105789.
15 V. Okatenko, L. Castilla-Amorós, D. C. Stoian, J. Vávra, A. Loiudice, R. Buonsanti, *J. Am. Chem. Soc.,* 2022, **144**, 10053−10063.
16 K. Zuraiqi, A. Zavabeti, J. Clarke-Hannaford, B.J. Murdoch, K. Shah, M.J.S. Spencer, C.F. McConville, T. Daeneke, K. Chiang, *Energy Environ. Sci.,* 2022, **15**, 595-600.
17 S. Frangini, A. Masi, *Intl. J. Hydrogen Energy,* 2016, **41**, 18739 – 18746.
18 C.G. Lee, H. Nakano, T. Nishina, I. Uchida, S. Kuro, *J. Electrochem. Soc.* 145 (1998) 2747.
19 E. Arato, E. Audasso, L. Barelli, B. Bosio, G. Discepoli, *J. Power Sources* 330 (2016) 18 – 27;
20 C.G. Lee, K. Yamada, Y. Hisamitsu, Y. Ono, I. Uchida, *Electrochem.,* 1999, **6**, 608-613.
21 R. Dedryvere, L. Gireaud, S. Grugeon, S. Laruelle, J.-M. Tarascon, D. Gonbeau, *J. Phys. Chem. B,* 2005, **109***,* 15868-15875.
22 C. Kranert, C. Sturm, R. Schmidt-Grund, M. Grundmann, *Sci. Reports,* 2016, **6**, 35964.
23 C.I.M. Rodríguez, M.A.L. Álvarez, J.J.F Rivera, G.G.C. Arízaga, C.R. Michel, *ECS J. Solid State Sci. Techn.,* 2019, **8**(7), Q3180-Q3186.
24 W. Priyantha, G. Radhakrishnan, R. Droopad, M. Passlack, *J. Crystal Growth,* 2011, **323**, 103–106.
25 K. Takechi, T. Shiga, T. Asaoka, *Chem. Commun.,* 2011, **47**, 3463-3465; J. Kim, A. Seong, Y. Yang, S. Joo, C. Kim, D.H. Jeon, L. Dai, G. Kim, *Nano Energy,* 2021, 82, 105741; S. Xu, S.K. Das, L.A. Archer, *RSC Adv.,* 2013, **3**, 6656–6660; J. Chen, K. Zou, P. Ding, J. Deng, C. Zha, Y. Hu, X. Zhao, J. Wu, J. Fan, Y. Li, *Adv. Mater.*, 2019, 31, 1805484; Y. Xing, Y. Yang, D. Li, M. Luo, N. Chen, Y. Ye, J. Qian, L. Li, D. Yang, F. Wu, R. Chen, S. Guo, *Adv. Mater.,* 2018, **30**, 1803124.
26 C. Xu, K. Zhang, D. Zhang, S. Chang, F. Liang, P. Yan, Y. Yao, T. Qu, J. Zhan, W. Ma, B. Yang, Y. Dai, X. Sun, *Nano Energy,* 2020, **68**, 104318.
27 Y. Wang, J. Liu, Y. Wang, Y. Wang, G. Zheng, *Nat. Commun*., 2018, **9**, 5034; M. Yang, S. Liu, J. Sun, M. Jin, R. Fu, S. Zhang, H. Li, Z. Sun, J. Luo, X. Liu, *Appl. Catal. B: Environ.,* 2022, **307**, 121145; S. Kaur, M. Kumar, D. Gupta, P.P. Mohanty, T. Das, S. Chakraborty, R. Ahuja, T.C. Nagaiah, *Nano Energy,* 2023, **109**, 108242; J. Li, L.-W. Chen, Y.-C. Hao, M. Yuan, J. Lv, A. Dong, S. Li, H. Gu, A.-X. Yin, W. Chen, P. Li, B. Wang, *Chem. Eng. J.,* 2023, **461**, 141865; H. Xie, H. Liao, S. Zhai, T. Liu, Y. Wu, F. Wang, J. Li, Y. Zhang, B. Chen, *Energy,* 2023, **263**, 125688.

